Electronic Supplementary Information for: CdSe/ZnS Quantum Dots as Sensors for the Local Refractive Index

Antoine Aubret[†], Anne Pillonnet[*,†], Julien Houel[†], Christophe Dujardin[†], and Florian Kulzer[*†]

December 4, 2015

This Supporting Information provides further information on the experimental setup and on the maximum-likelihood analysis of fluorescence decay curves, a discussion of the precision that can be achieved when determining the ON-state fluorescence decay rate γ_1 from decay curves derived from high-intensity bins of a timetrace, and the details of the calculation of the effective refractive index $\bar{n}$ according to the Bruggeman effective medium approach.

Contents

[*]To whom correspondence should be addressed: anne.pillonnet@univ-lyon1.fr, florian.kulzer@univ-lyon1.fr
[†]Institut Lumière Matière, CNRS UMR5306
Université Lyon 1, Université de Lyon
69622 Villeurbanne CEDEX, France

1 Time-Resolved Confocal Microscopy

Our home-built confocal microscope, shown schematically in Figure S1a, is described in detail in Ref. S1. Briefly, a Ti:sapphire oscillator (Tsunami, Newport/Spectra Physics 3960-M3BB) provided a pulsed near-infrared beam, $\lambda_{\text{center}} = 892\,\text{nm}$, with a pulse duration of about 45 fs at a repetition rate of 80 MHz. A combined β-barium borate frequency doubler/pulse picker unit (Spectra Physics 3980) then allowed to obtain 200 fs pulses centered around 446 nm at repetition rates that could accommodate the relaxation dynamics between two successive pulses (4 MHz for QD525 and 2 MHz for QD655).

A small part of the resulting 446 nm excitation beam was split off to provide reference pulses to a photodiode; the major fraction was directed toward a microscope objective (Nikon, CFI LU PlanFluor EPI P 100 $\times$, NA 0.9) to focus it, after suitable attenuation by neutral density filters, on the objective-facing, QD-coated surface of the substrate. The substrate was scanned through the (near) diffraction-limited focus by means of a closed-loop stabilized XYZ-piezo stage (Mad City Labs, NanoDrive). The luminescence photons were collected by the same objective and separated from residual laser light and other background contributions by appropriate bandpass filters (Thorlabs, FES0550, FEL0500, FB650-40) before being focused on single photon counting avalanche photodiode (APD, Perkin Elmer, SPCM-AQRH-14), whose active area served as the detection pinhole. All lenses used in the optical path way were achromatic doublets. Time-correlated single photon counting (TCSPC) electronics (Picoquant, TimeHarp 200) allowed to record the arrival times of all detected photons relative to the laser pulses impinging on the reference diode with an internal temporal resolution better than 40 ps. The overall instrumental response function (IRF) had a width of about 0.6 ns. Control of the piezo stage either permitted to obtain a total intensity and lifetime image of a certain region of the sample, with dimensions of typically several tens of microns in both lateral directions, or to place an isolated nanoparticle in the focus and to study its luminescence dynamics in more detail. The observation of isolated nanoemitters was corroborated by on/off-blinking as exemplified by the luminescence intensity timetrace shown in Figure S1 (b). For each substrate, we chose approximately 10 individual QDs and recorded their luminescence decay curve at low excitation powers corresponding to free-space peak intensities of $50\,\text{W/cm}^2$ in the focus of the microscope objective. A flip mirror furthermore allowed to direct the collected luminescence to a spectrograph (Andor, Shamrock SR500) equipped with an electron-multiplying charge-coupled device (EMCCD) camera (Andor, DU970P-UVB,USB) for verification of the luminescence spectra. A stand-alone CCD video camera (Allied Vision, Pike F421B) was used for alignment and focusing, as well as for quick surveys of the samples.

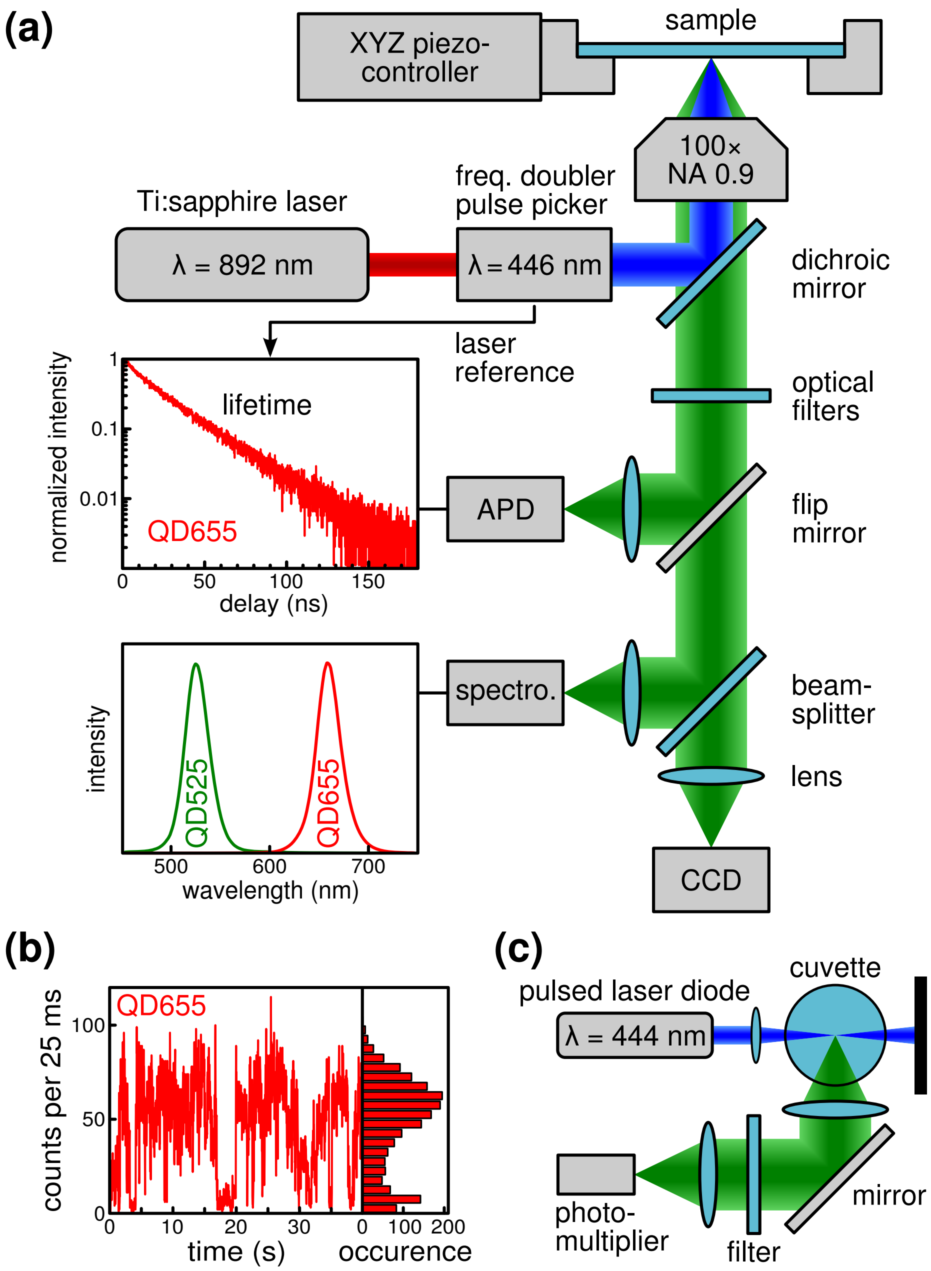

Figure S1: Schematic diagrams of experimental setups for lifetime measurements and illustrative data. (a) Confocal microscopy on single nanoparticles dispersed on dielectric substrates: Frequency doubled 45 fs pulses of a Ti:sapphire laser were focused on the substrate surface after positioning isolated nanocrystals in the focus by means of an XYZ piezo stage. The collected luminescence was filtered, focused on a avalanche photodiode (APD) and analyzed by time-correlated single photon counting (TCSPC) electronics to obtain luminescence lifetime curves like the example shown above (QD655, excitation intensity 50 W/cm^2 at 446 nm, integration time 100 s). A spectrograph/EMCCD combination allowed to verify the emission spectra of both QD species. (b) Intensity timetrace and corresponding histogram of a single QD525 excited at an intensity of 50 W/cm^2; blinking events, *i. e.*, transitions between two distinct regimes of emission count rates, are clearly visible. (c) Lifetime measurements on QDs in solutions were performed by focusing the emission of a pulsed laser diode into the QD solution and registering the collected luminescence photons with a photomultiplier coupled to TCSPC electronics.

2 Maximum-Likelihood Estimation of Fluorescence Decay Rates

2.1 Likelihood Function, Kullback–Leibler Divergence, and Poisson Deviance

We used maximum-likelihood (ML) analysis [S2–S6] to fit our measured fluorescence decay curves because this efficient and unbiased approach to parameter estimation is preferable to the widely used χ^2 minimization, especially for decay histograms containing a small number of photons [S7]. The ML analysis of fluorescence lifetime data starts with a decay histogram comprised of n channels, where each channel $i = 1, 2, \ldots, n$ contains the number c_i of counts detected with a delay between $(i-1)\,t_\mathrm{b}$ and $i\,t_\mathrm{b}$ relative to the excitation laser pulse; t_b is the histogram bin time. A given model, *e. g.* mono- or biexponential decay, has its associated vector $\boldsymbol{\theta} = (\theta_1, \ldots, \theta_m)$ of m parameters such as decay rate(s), amplitude(s), and background contribution. The likelihood function L is the joint probability of observing a given sequence of channel counts $\{c_i\}$ and can be written as [S4]

$$L\big(c_1, \ldots, c_n|\boldsymbol{\theta}\big) = \prod_{i=1}^{n} p(c_i|\boldsymbol{\theta}) \qquad , \tag{S1}$$

where $p(c_i|\boldsymbol{\theta})$ is the conditional probability of detecting c_i counts in the i-th channel for a certain choice of model parameters $\boldsymbol{\theta}$. The parameter vector $\hat{\boldsymbol{\theta}}$ that maximizes the likelihood function L represents the maximum-likelihood estimation (MLE) of the model parameters for the data set $\{c_i\}$. For practical purposes it is usually $\ln(L)$ that is maximized by parameter variation, as the transition to logarithms allows to rewrite the product in Eq. (S1) as a sum of $\ln(p_i)$ terms. Analytic expressions for $\hat{\boldsymbol{\theta}}$ can be found in some cases by setting the derivatives of $\ln(L)$ with respect to the parameters θ_i to zero and solving the resulting system of equations for the m unknown parameters; alternatively, a numerical search for a maximum in $\boldsymbol{\theta}$ space can be performed if a given model is not amenable to analytic resolution of the ML conditions.

An approach equivalent to maximizing the likelihood function L consists in finding $\hat{\boldsymbol{\theta}}$ by minimization of a statistical measure $D(\boldsymbol{\theta})$ that quantifies the discrepancy between the data set $\{c_i\}$ and the corresponding predictions $\{g_i(\boldsymbol{\theta})\}$ of the model. A possible choice for D is the Kullback − Leibler divergence [S5], which, in the notation adopted above, is given by

$$D_\mathrm{KL}(\boldsymbol{\theta}) = 2\sum_{i=1}^{n} c_i \,\ln\left(\frac{c_i}{g_i(\boldsymbol{\theta})}\right) \qquad . \tag{S2}$$

An alternative statistical measure for Poisson-distributed data such as photon counting histograms is the Poisson deviance [S4]

$$D_\mathrm{Poiss}(\boldsymbol{\theta}) = 2\sum_{i=1}^{n}\Big\{c_i \,\ln\big[c_i/g_i(\boldsymbol{\theta})\big] - \big[c_i - g_i(\boldsymbol{\theta})\big]\Big\} \qquad , \tag{S3}$$

which is identical to D_KL in the limit of an infinite number of detected photons, when the term $c_i - g_i(\boldsymbol{\theta})$ tends to zero for unbiased models. Minimization of $D_\mathrm{KL}(\boldsymbol{\theta})$ and $D_\mathrm{Poiss}(\boldsymbol{\theta})$ was performed by the Nelder − Mead downhill simplex algorithm [S8] as implemented by Scilab (www.scilab.org). We found that both statistical measures converged to the same MLE $\hat{\boldsymbol{\theta}}$ for our data sets, with D_Poiss showing somewhat faster convergence if the minimization was started with suboptimal initial guesses for the model parameters.

2.2 Multinomial Distributions for Decay Histograms

The multinomial probability of observing the data set $\{c_i\}$ for the n photon counting channels is given by [S6]

$$P(c_1, \ldots, c_n|\boldsymbol{\theta}) = \frac{N!}{\prod_{i=1}^{n} c_i!} \prod_{i=1}^{n} p_i(\boldsymbol{\theta})^{c_i} \qquad , \tag{S4}$$

where $N = \sum_{i=1}^{n} c_i$ is the total number of detected photons and $p_i(\boldsymbol{\theta})$ denotes the probability that a photon will fall into detection channel i; these probabilities are normalized to the detection window such that $\sum_{i=1}^{n} p_i(\boldsymbol{\theta}) = 1$. The relationship between the model function $g_i(\boldsymbol{\theta})$ as defined above and the probabilities from Eq. (S4) is straightforward, $g_i(\boldsymbol{\theta}) = N \cdot p_i(\boldsymbol{\theta})$, which can be substituted directly into Eqs. (S2) and (S3) for the minimization procedure. We used the multinomial model of Eq. (S4) because it offers certain advantages over an approach based on Poisson distributions [S6].

The probabilities $p_i(\boldsymbol{\theta})$ can be calculated for a given decay model as [S6]

$$p_i(\boldsymbol{\theta}) = \int\limits_{\Delta_i} R(t|\boldsymbol{\theta})\, dt \qquad , \tag{S5}$$

where Δ_i is the temporal interval associated with the i-th counting channel and $R(t|\boldsymbol{\theta})\, dt$ is the probability of detecting an emitted photon between t and $t + dt$ after the excitation pulse.

2.3 Monoexponential Decay Curves

The probability density $R(t|\gamma, T)$ of a background-free monoexponential decay with rate γ is [S6]

$$R(t|\gamma, T) = \gamma \exp\bigl(-\gamma t\bigr)\, \frac{1}{1 - \exp(-\gamma T)} \qquad , \tag{S6}$$

which has been renormalized to the overall temporal width T of the detection window. Given data acquisition with n channels of equal width (duration) $t_{\mathrm{b}} = T/n$, this means that the probability of a photon being detected in channel i, Eq. (S5), takes the following form [S6]:

$$p_i(\gamma, T, n) = \int\limits_{(i-1)T/n}^{iT/n} R(t|\gamma, T)\, dt = \exp\bigl(-i\gamma T/n\bigr)\, \frac{\exp(\gamma T/n) - 1}{1 - \exp(-\gamma T)} \tag{S7}$$

For monoexponential decay on non-zero background, the probability of photon detection in channel i changes to [S6]

$$p_i(\gamma, b, T, n) = \frac{b}{n} + \bigl(1 - b\bigr)\, p_i(\gamma, T, n) \qquad , \tag{S8}$$

where b is the relative background contribution. Consequently, we used the model function derived from Eq. (S8),

$$g_i(\gamma, b) = N p_i(\gamma, b, T, n) = \frac{Nb}{n} + N\bigl(1 - b\bigr)\, p_i(\gamma, T, n) \qquad , \tag{S9}$$

to find the ML parameters for monoexponential decay curves by minimizing D_{KL} or D_{Poiss} as defined in Eqs. (S2) and (S3). The results of applying the MLE procedure to monoexponential decay curves constructed from photons selected from (predominantly) ON bins in single-QD emission are discussed in Sec. 3 below.

2.4 Biexponential Decay Curves

The probability of photon detection in the i-th channel for biexponential decay curves on non-zero background is [S6]

$$p_i(\gamma_1, \gamma_2, a, b, T, n) = \frac{b}{n} + \bigl(1 - b\bigr)\, \Bigl[a\, p_i(\gamma_1, T, n) + \bigl(1 - a\bigr)\, p_i(\gamma_2, T, n)\Bigr] \qquad , \tag{S10}$$

where γ_1 and γ_2 are the two decay rates, a is the relative strength of the γ_1 component (not the population fraction [S9]), and b the fraction of background counts. The model function for the MLE of the biexponential decay parameters is then given by $g_i(\gamma_1, \gamma_2, a, b) = N \cdot p_i(\gamma_1, \gamma_2, a, b, T, n)$, which was used to obtain all the γ_1 values reported in the main article for biexponential decay curves of single QDs on substrates. (Our convention is to denote as γ_1 the slower decay component thought to be associated with emission of the "on" state.)

2.5 Biexponential Decay Curves with Normally Distributed Rates

All decay time histograms measured form QD ensembles in solution deviated significantly from biexponential behavior. Gaussian distributions [S10, S11] of the decay rates for both on- and off-states, γ_1 and γ_2, respectively, were therefore introduced to allow for the size and shape distributions of the QDs, which means replacing Eq. (S10) by

$$p_i = \frac{b}{n} + \frac{1-b}{\sqrt{2\pi}} \int_0^\infty \left\{ \frac{a}{\sigma_1} \exp\left[-\frac{(\gamma-\gamma_1)^2}{2\,\sigma_1^2} \right] + \frac{1-a}{\sigma_2} \exp\left[-\frac{(\gamma-\gamma_1)^2}{2\,\sigma_1^2} \right] \right\} p_i(\gamma, T, n)\, d\gamma \quad , \quad \text{(S11)}$$

where σ_1 and σ_2 are the standard deviations of the Gaussian rate distributions for on- and off-state, respectively, and $p_i(\gamma, T, n)$ is given by Eq. (S7). Note that an approximation was introduced in the normalization of Eq. (S11); the exact normalization factors for the two components are

$$\frac{\sqrt{2}}{\sqrt{\pi}\sigma_1} \left[1 + \operatorname{erf}\left(\frac{\gamma_1}{\sqrt{2}\,\sigma_1} \right) \right]^{-1} \quad \text{and} \quad \frac{\sqrt{2}}{\sqrt{\pi}\sigma_2} \left[1 + \operatorname{erf}\left(\frac{\gamma_2}{\sqrt{2}\,\sigma_2} \right) \right]^{-1} \quad , \quad \text{(S12)}$$

respectively. However, the γ_1/σ_1 ratios were found to be $\gtrsim 4$ for QD525 and $\gtrsim 3$ for QD655, which means that for both QD species the error functions in the above expressions can be approximated as unity, given that $\operatorname{erf}\big(4/\sqrt{2}\big) \approx 0.99994 \approx 1$ and $\operatorname{erf}\big(3/\sqrt{2}\big) \approx 0.997 \approx 1$. Even for the fast component, where we found $\gamma_2/\sigma_2 \gtrsim 2$, the approximation $\operatorname{erf}\big(2/\sqrt{2}\big) \approx 0.954 \approx 1$ remains acceptable. The two normalization factors of Eq. (S12) can therefore be simplified to $1/\big(\sqrt{2\pi}\sigma_1\big)$ and $1/\big(\sqrt{2\pi}\sigma_2\big)$; the common factor of $1/\sqrt{2\pi}$ has been taken out of the integral in Eq. (S11). Typically, the contribution of the fast component constituted a few percent of the total number of luminescence photons, making it possible to find accurate values of the γ_1 (slow) component for each set of QDs. Tables S1 and S2 summarize the ML parameters estimated following Eq. (S11) for the fluorescence decay curves measured for QD525 and QD655, respectively, in water and sucrose solutions.

3 Fluorescence Decay Curves Constructed from ON Bins

Figure S2a shows part of a fluorescence intensity timetrace of a single QD525 on BK7, illustrating power-law blinking with alternating ON and OFF periods whose durations are broadly distributed. The corresponding histogram of count rates for the full trace, Figure S2b, reveals an OFF intensity level of $\lesssim 1\,\text{count}/(10\,\text{ms})$ and an ON state reaching $\sim 30\,\text{counts}/(10\,\text{ms})$ on average. A threshold of $24\,\text{counts}/(10\,\text{ms})$, indicated by the dashed line in Figures S2ab, was used for selecting high-level bins that can be expected to be dominated by ON state emission. As can be seen in Figures S2cd, decay curves constructed from high-level bins do indeed exhibit monoexponential behavior without noticeable contributions of the fast decay component (γ_2) associated with the OFF state. As expected, the uncertainty of the fit parameter for the shorter trace, $\gamma_1 = (3.61 \pm 0.02) \cdot 10^{-2}\,\text{ns}^{-1}$, is larger than what can be achieved when using all ON bins of the trace, $\gamma_1 = (3.627 \pm 0.009) \cdot 10^{-2}\,\text{ns}^{-1}$.

Table S1: Fluorescence dynamics of QD525 in water and in sucrose solutions of varying refractive index; decay curves were interpreted with a biexponential model, Eq. (S11), whose principal rates γ_1 and γ_2 exhibit Gaussian distributions with standard deviations of σ_1 and σ_2, respectively.

refractive index	γ_1 $[\mathrm{ns}^{-1}]$	σ_1 $[\mathrm{ns}^{-1}]$	γ_2 $[\mathrm{ns}^{-1}]$	σ_2 $[\mathrm{ns}^{-1}]$
1.330	$4.89 \cdot 10^{-2}$	$1.01 \cdot 10^{-2}$	$2.60 \cdot 10^{-1}$	$7.22 \cdot 10^{-3}$
1.347	$5.13 \cdot 10^{-2}$	$1.27 \cdot 10^{-2}$	$3.05 \cdot 10^{-1}$	$5.57 \cdot 10^{-5}$
1.366	$5.31 \cdot 10^{-2}$	$1.18 \cdot 10^{-2}$	$2.67 \cdot 10^{-1}$	$9.54 \cdot 10^{-2}$
1.371	$5.42 \cdot 10^{-2}$	$1.22 \cdot 10^{-2}$	$2.87 \cdot 10^{-1}$	$1.72 \cdot 10^{-2}$
1.410	$5.69 \cdot 10^{-2}$	$1.24 \cdot 10^{-2}$	$3.27 \cdot 10^{-1}$	$9.33 \cdot 10^{-2}$
1.420	$5.92 \cdot 10^{-2}$	$1.32 \cdot 10^{-2}$	$3.05 \cdot 10^{-1}$	$1.14 \cdot 10^{-1}$
1.440	$6.15 \cdot 10^{-2}$	$1.46 \cdot 10^{-2}$	$3.07 \cdot 10^{-1}$	$1.07 \cdot 10^{-1}$
1.455	$6.28 \cdot 10^{-2}$	$1.43 \cdot 10^{-2}$	$3.32 \cdot 10^{-1}$	$1.30 \cdot 10^{-1}$
1.460	$6.48 \cdot 10^{-2}$	$1.60 \cdot 10^{-2}$	$3.65 \cdot 10^{-1}$	$1.61 \cdot 10^{-1}$

Table S2: Fluorescence dynamics of QD655 in water and in sucrose solutions of varying refractive index; decay curves were interpreted with a biexponential model, Eq. (S11), whose principal rates γ_1 and γ_2 exhibit Gaussian distributions with standard deviations of σ_1 and σ_2, respectively.

refractive index	γ_1 $[\mathrm{ns}^{-1}]$	σ_1 $[\mathrm{ns}^{-1}]$	γ_2 $[\mathrm{ns}^{-1}]$	σ_2 $[\mathrm{ns}^{-1}]$
1.330	$2.59 \cdot 10^{-2}$	$8.60 \cdot 10^{-3}$	$1.02 \cdot 10^{-1}$	$3.18 \cdot 10^{-2}$
1.347	$2.74 \cdot 10^{-2}$	$8.70 \cdot 10^{-3}$	$1.09 \cdot 10^{-1}$	$3.88 \cdot 10^{-2}$
1.366	$2.80 \cdot 10^{-2}$	$9.50 \cdot 10^{-3}$	$1.21 \cdot 10^{-1}$	$3.74 \cdot 10^{-2}$
1.371	$2.82 \cdot 10^{-2}$	$8.95 \cdot 10^{-3}$	$1.02 \cdot 10^{-1}$	$2.95 \cdot 10^{-2}$
1.410	$3.03 \cdot 10^{-2}$	$1.01 \cdot 10^{-2}$	$1.50 \cdot 10^{-1}$	$4.47 \cdot 10^{-5}$
1.420	$3.06 \cdot 10^{-2}$	$9.63 \cdot 10^{-3}$	$1.22 \cdot 10^{-1}$	$3.87 \cdot 10^{-2}$
1.440	$3.22 \cdot 10^{-2}$	$1.08 \cdot 10^{-2}$	$1.90 \cdot 10^{-1}$	$3.83 \cdot 10^{-4}$
1.453	$3.29 \cdot 10^{-2}$	$1.09 \cdot 10^{-2}$	$2.11 \cdot 10^{-1}$	$1.66 \cdot 10^{-4}$
1.455	$3.23 \cdot 10^{-2}$	$1.02 \cdot 10^{-2}$	$1.24 \cdot 10^{-1}$	$3.01 \cdot 10^{-2}$

The uncertainties $\delta\gamma_1$ are crucial for the estimation of the detection limit N_{lim} as given by Eq. (4) of the main article. We therefore used the bootstrap method [S8] to determine the uncertainties of the decay parameters that we obtained from the MLE analysis detailed in Section 2. The bootstrap method consists in creating synthetic data sets from a given decay curve by randomly selecting N_0 points from the experimental data. This random selection process is implemented as drawing with replacement, which means that each data point has the same probability to be chosen in each draw, irrespective of whether it has already been selected in earlier draws. Each synthetic data set derived in this manner will therefore have a random fraction of the original data points missing ($\sim 37\,\%$ on average), while a number of the included data points is duplicated (and, on increasingly rare occasions, triplicated, quadrupled, *etc.*) such that the overall length N_0 of the original data set is conserved. The ensemble of synthetic data sets thus obtained is then subjected to the same analysis as the measured data; the resulting distributions of the fit parameters furnish a good estimation for how precisely the parameters can be known from the data, provided that the measured data points can be assumed to be independent and identically distributed [S8]. All values of N_{lim} reported in the main article are based on uncertainties $\delta\gamma_1$ obtained from the sample standard deviations of bootstrap estimations with 500 synthetic data sets for each decay curve. We furthermore verified that the mean value of γ_1 obtained from the synthetic data sets is consistent with the

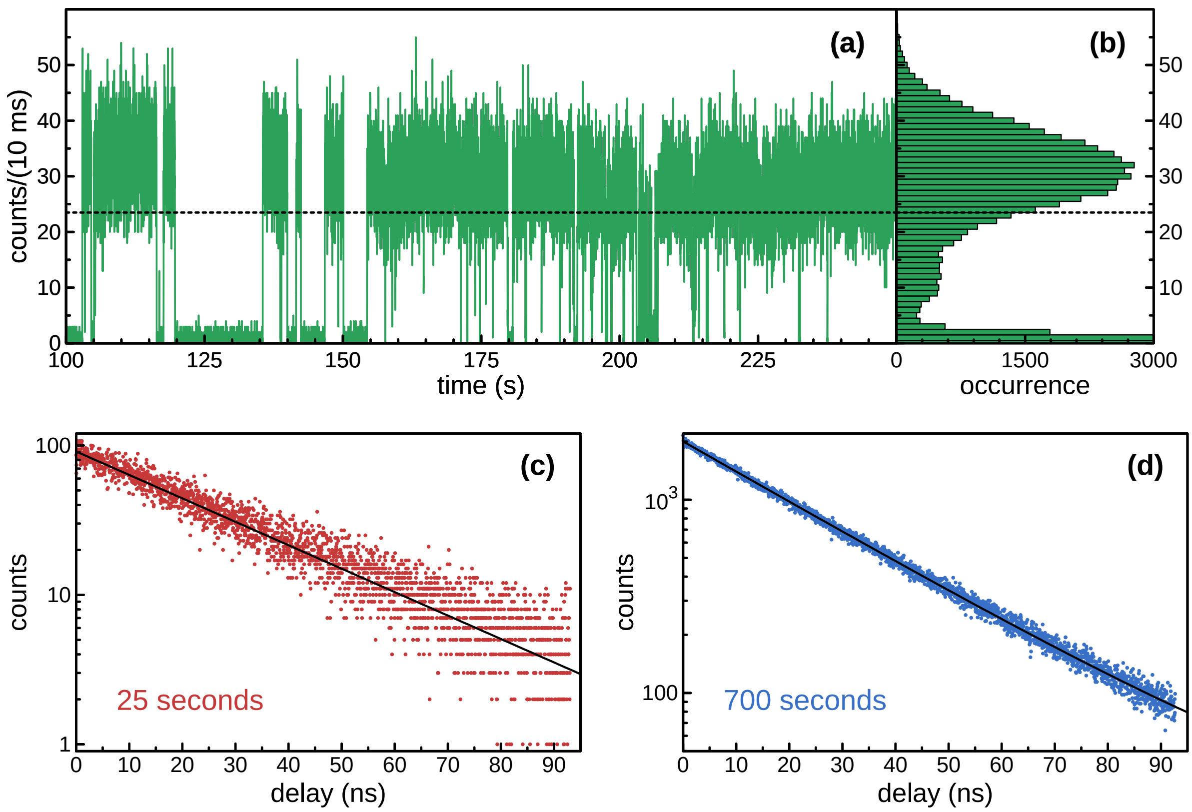

Figure S2: Fluorescence intensity timetraces and decay curves of a single QD525 on BK7. (a) Part of a 700 s timetrace, showing the succession of ON and OFF periods (blinking) in the fluorescence emission of a single QD525. The trace was generated by binning photon arrival time data (instrumental resolution: 100 ns) into aligned intervals of 10 ms duration. The horizontal dashed line indicates the threshold subsequently used to select timebins dominated by ON photons. (b) Histogram of intensity levels observed in the full timetrace. The abscissa of the histogram is oriented vertically so that it coincides with the intensity axis of the trace in (a); the horizontal axis marks the number of occurrences for each intensity level. (The two bars not fully visible in the plot correspond to 7799 occurrences of 0 counts and 5093 occurrences of 1 count per timebin, respectively.) (c) Fluorescence decay histogram constructed from high-level timebins that occurred during the first 25 seconds of the measurement (dots). The solid line represents a monoexponential fit with a decay rate of $\gamma_1 = (3.61 \pm 0.02) \cdot 10^{-2}\,\mathrm{ns}^{-1}$. (d) Fluorescence decay curve constructed from all high-level bins of the entire 700 s timetrace (dots). The line shows the monoexponential fit with $\gamma_1 = (3.627 \pm 0.009) \cdot 10^{-2}\,\mathrm{ns}^{-1}$ and a background of (16 ± 1) counts.

result of the ML analysis of the corresponding original data set.

4 The Bruggeman Effective Medium Approach

The Bruggeman effective medium approach treats each constituting phase of a mixed medium equally as an inclusion in the effective medium itself [S12], which avoids the often somewhat arbitrary distinction between "host" and "guest" components that would otherwise have to be introduced. We apply this approach to a sphere of interaction with radius R, centered on the QD core, which is occupied by air and the part of the substrate intersecting with the interaction sphere in the shape of a spherical cap. The corresponding effective refractive index $\bar{n}$ is then obtained [S13] as the positive real solution of the equation

$$f_\mathrm{s} \cdot \frac{n_\mathrm{s}^2 - \bar{n}^2}{n_\mathrm{s}^2 + 2\bar{n}^2} + \left(1 - f_\mathrm{s}\right) \cdot \frac{n_\mathrm{air}^2 - \bar{n}^2}{n_\mathrm{air}^2 + 2\bar{n}^2} = 0 \qquad , \tag{S13}$$

where n_s and n_air are the refractive indices of the substrate and of air, respectively. The volume fraction f_s of the substrate in the interaction sphere was calculated by dividing the volume of a spherical cap of height h_s,

$$V_\mathrm{s} = \pi h_\mathrm{s}^2 \left(R - h_\mathrm{s}/3\right) \qquad , \tag{S14}$$

by the total volume of the interaction sphere, $V = \frac{4}{3}\pi R^3$. The height h_s of the spherical cap occupied by the substrate is $h_\mathrm{s} = R - d$, where d is the distance from the core-centered emission dipole to the surface of the substrate.

References

[S1] F. Ayela, M. Medrano-Muñoz, D. Amans, C. Dujardin, T. Brichart, M. Martini, O. Tillement and G. Ledoux, *Phys. Rev. E*, 2013, **88**, 043016.

[S2] P. Hall and B. Selinger, *J. Phys. Chem.*, 1981, **85**, 2941–2946.

[S3] P. Hall and B. Selinger, *Z. Phys. Chem. Neue Fol.*, 1984, **141**, 77–89.

[S4] Z. Bajzer, T. M. Therneau, J. C. Sharp and F. G. Prendergast, *Eur. Biophys. J. Biophys. Lett.*, 1991, **20**, 247–262.

[S5] M. Köllner, *Inst. Phys. Conf. Ser.*, 1992, **1992**, 151–154.

[S6] M. Köllner and J. Wolfrum, *Chem. Phys. Lett.*, 1992, **200**, 199–204.

[S7] J. Kim and J. Seok, *Opt. Express*, 2013, **21**, 6061–6075.

[S8] W. H. Press, S. A. Teukolsky, W. T. Vetterling and B. P. Flannery, *Numerical Recipes: The Art of Scientific Computing*, Cambridge University Press, Cambridge, 3rd edn, 2007.

[S9] A. F. van Driel, I. S. Nikolaev, P. Vergeer, P. Lodahl, D. Vanmaekelbergh and W. L. Vos, *Phys. Rev. B*, 2007, **75**, 035329.

[S10] B. R. Fisher, H. J. Eisler, N. E. Stott and M. G. Bawendi, *J. Phys. Chem. B*, 2004, **108**, 143–148.

[S11] C. Belacel, B. Habert, F. Bigourdan, F. Marquier, J. P. Hugonin, S. M. de Vasconcellos, X. Lafosse, L. Coolen, C. Schwob, C. Javaux, B. Dubertret, J. J. Greffet, P. Senellart and A. Maitre, *Nano Lett.*, 2013, **13**, 1516–1521.

[S12] D. E. Aspnes, *Am. J. Phys.*, 1982, **50**, 704–709.

[S13] A. Pillonnet, P. Fleury, A. I. Chizhik, A. M. Chizhik, D. Amans, G. Ledoux, F. Kulzer, A. J. Meixner and C. Dujardin, *Opt. Express*, 2012, **20**, 3200–3208.